CrossMark

Interface reduction methods for mechanical systems with elastohydrodynamic lubricated revolute joints

Andreas Krinner[1] · Daniel J. Rixen[1]

Abstract In this contribution, three different reduction methods for elastic structures with lubricated interfaces are presented and compared with each other. While for the first two methods, classical reduction strategies from component mode synthesis are applied, for the third method, a dual reduction basis is used, consisting of vibration modes of the free floating structure, attachment modes and residual modes. Within this new dual approach, it is shown how the residual modes can be obtained by applying pressure distributions of analytical solutions of the hydrodynamic equations. The described methods are compared for two classical simulation example—for a one-sided elastohydrodynamic lubricated joint of a slider–crank mechanism in a floating frame of reference formulation as well as for an elastic rotor in a flexible journal bearing.

Keywords Elastohydrodynamics · Interface reduction · Mode synthesis · Residual modes · Bearing simulation

1 Introduction

Elastohydrodynamic (EHD) lubricated joints can be found in various applications of automotive or rotor dynamics, e.g. in the crank shaft connecting rod link of a slider–crank mechanism of a combustion engine [3, 14, 20]. Their detailed numerical simulation gives information as regards maximal pressure, minimal height, cavitation zones or stability limits. The pressure distribution is usually calculated by a numeric discretization of the REYNOLDS equation. For highly loaded bearings, the local deformation of the structure at the interface strongly affects the pressure distribution in the fluid film. Therefore, a detailed representation of the lubricated interface of an elastic structure is required leading to a large number

✉ A. Krinner
andreas.krinner@tum.de

D.J. Rixen
rixen@tum.de

[1] Chair of Applied Mechanics, Technical University of Munich, Boltzmannstraße 15, 85748 Garching, Germany

of elastic degrees of freedom. General examples for EHD lubricated joints can be found in [23, 24].

For further simulation purposes like a flexible multi-body simulation, a reduction of the elastic structure with the large coupling interface is inevitable. In the context of component mode synthesis (CMS), the classical approaches are based on a static or a modal interface reduction, as described in [5]. On the basis of CMS, interface reduction methods for systems with fluid–structure interaction are outlined in [12, 13]. However, dual approaches can also be used, which account for interface loads by the use of attachment modes. On this basis, a time dependent parametric model order reduction scheme for systems with varying loads is given in [22]. In the context of EHD lubrication, a dual approach is followed in [9, 10], where a set of basis vectors coming from a static analysis at different load regimes is applied for the interface reduction of line and circular point contacts, respectively.

In this paper, we apply three different reduction schemes for structures with lubricated interfaces and discuss their numerical and computational efficiency in the context of a multi-body simulation by using a floating frame of reference formulation. The first method represents a classical CRAIG–BAMPTON [1] reduction of the structure without considering the lubricated interface in particular. In the second method, which is already applied by [19], first, a CRAIG–BAMPTON reduction is applied to the elastic structure in order to maintain the degrees of freedom of the lubricated interface. In a second step, the already reduced structure is further reduced by a second CRAIG–BAMPTON step. The third method, published in [15], makes use of a dual reduction strategy as proposed in [7]. Within this concept, load dependent interface modes are used to represent the elastic deformation of the interface due to pressure forces.

Results for the behavior of the three methods are presented for two classical simulation examples: the first one is a slider crank mechanism with a flexible connecting rod modeled by a Finite Element (FE) discretization. The crank shaft and the rod are connected by a cylindrical EHD lubricated joint. The second one is an elastic rotor with unbalance, which rotates in a flexible journal bearing.

The structure of the paper is as follows: in Sect. 2, a brief introduction to the hydrodynamic equations including REYNOLDS equation, joint kinematics, cavitation condition and force calculation is given. In Sect. 3, the three reduction methods are outlined. In Sect. 4, the first simulation example of a flexible slider–crank mechanism with a lubricated joint is described and global simulation outputs for the different methods are compared. In Sect. 5, the second simulation example of an elastic rotor in a flexible bearing is investigated. A conclusion is given in Sect. 6.

2 Hydrodynamic equations

In this section, the hydrodynamic equations for the pressure calculation in an elastohydrodynamic lubricated cylindrical joint are given. For a more detailed description, it is referred to [11, 17]. It is noted that in the following, isoviscous and isothermal lubricant properties are assumed, even though the viscosity is sensitive to changes in pressure and temperature. However, since the later described reduction approaches remain unaffected by the fluid behavior, constant fluid properties are assumed for simplicity.

2.1 Pressure calculation

The pressure is computed by a finite element discretization of the REYNOLDS equation. For a cylindrical, flexible joint, the kinematics needed for the REYNOLDS equation are derived

Fig. 1 Notations in the fluid domain
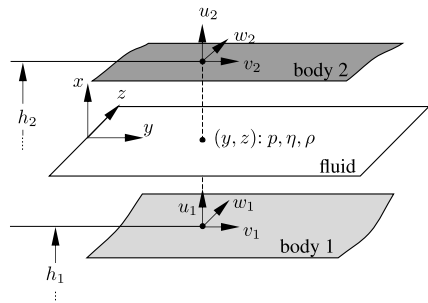
in detail. During the pressure computation, a steady-state cavitation condition, also known as REYNOLDS condition, is applied in order to avoid negative pressures in the fluid film.

2.1.1 REYNOLDS *equation*

For the lubricated contact depicted in Fig. 1, the pressure distribution in the fluid film between two bodies can be calculated by the REYNOLDS equation when the fluid film is thin and fluid inertia is neglected. To simplify the presentation, but without loss of generality, it is further assumed that fluid viscosity η and density ρ do neither depend on pressure nor on temperature. Then the REYNOLDS approach gives the following partial differential equation for the pressure in the fluid film $h(y, z) = h_2 - h_1$ between the two bodies in the two-dimensional fluid domain $\Omega_f \subset \mathbb{R}^2$ with descriptive coordinates (y, z) (see for instance [11]):

$$\underbrace{-\frac{\partial}{\partial y}\left(\frac{h^3 \rho}{12\eta}\frac{\partial p}{\partial y}\right) - \frac{\partial}{\partial z}\left(\frac{h^3 \rho}{12\eta}\frac{\partial p}{\partial z}\right)}_{q_{\text{poiseuille}}} = \underbrace{-\frac{\partial}{\partial y}\left(\rho h \frac{v_1 + v_2}{2}\right)}_{-q_{\text{couette}}} \underbrace{-\rho\frac{\partial h}{\partial t}}_{-q_{\text{squeeze}}} \underbrace{-h\frac{\partial \rho}{\partial t}}_{-q_{\text{expansion}}} \tag{1}$$

where u_i and v_i are the absolute velocities of the interface of body i ($i \in \{1, 2\}$) in the local normal and tangential direction, respectively. For simplicity, the velocity w_i in z-direction is not considered here, as its change is usually negligible in classical bearings. The POISEUILLE term $q_{\text{poiseuille}}$ describes the flow driven by the pressure gradient, the COUETTE term q_{couette} describes the flow due to the movement of surfaces in the tangential y-direction, the squeeze term q_{squeeze} describes the flow due to squeezing motion and the local expansion term $q_{\text{expansion}}$ describes the change of density. The flow $q_{\text{expansion}}$ will be used to impose a steady-state cavitation condition in the one of the following subsections. The squeeze term of Eq. (1) is expressed in terms of the local normal velocities u_i, tangential velocities v_i and derivatives of the heights h_i with respect to y, see [11]:

$$\frac{\partial h}{\partial t} = u_2 - v_2\frac{\partial h_2}{\partial y} - u_1 + v_1\frac{\partial h_1}{\partial y}. \tag{2}$$

2.1.2 *Joint kinematics*

For a cylindrical joint with flexible bearing shell and rigid shaft, the local kinematic quantities can be derived according to Fig. 2. The procedure is explained for a two-dimensional problem, but it can without difficulty be extended to the three-dimensional case. In the cylindrical bearing, the local coordinates ($y = R\varphi, z$) are used for the description of the fluid

Fig. 2 Kinematics in cylindrical joint
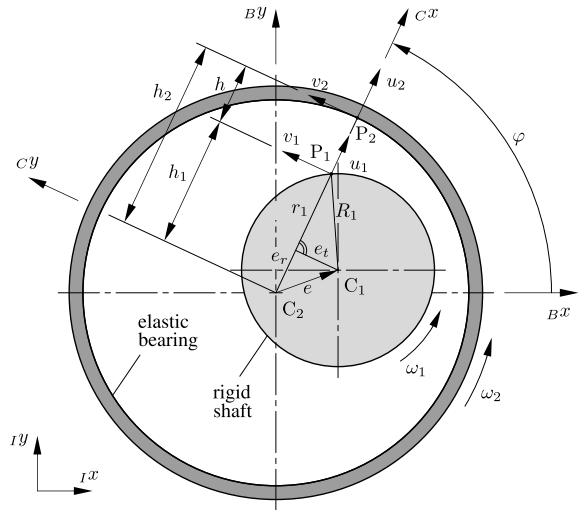
domain. The joint kinematics is described in the frame $(_B x,\ _B y)$, which is fixed to the bearing shell. For the REYNOLDS equation, local quantities are needed, i.e. the velocities and heights have to be transformed into the local frame $(_C x,\ _C y)$ of cylindric coordinates. For the eccentricity between the two center points C_1 and C_2 follows:

$$_B \mathbf{e} = \begin{pmatrix} e_x \\ e_y \end{pmatrix} \rightarrow_C \mathbf{e} = \begin{pmatrix} e_r \\ e_t \end{pmatrix} = \begin{pmatrix} e_x \cos(\varphi) + e_y \sin(\varphi) \\ -e_x \sin(\varphi) + e_y \cos(\varphi) \end{pmatrix}. \tag{3}$$

According to Fig. 2, the following local heights h_1 and h_2 can be derived for the two points P_1 and P_2, respectively:

$$h_1(y, z) = e_r(y, z) + \sqrt{R_1^2 - e_t^2(y, z)} \approx e_r(y, z) + R_1 \tag{4}$$

$$h_2(y, z) = R_2 + \delta_r(y, z), \tag{5}$$

where $\delta_r(y, z)$ describes the elastic deformation of the bearing shell in the radial direction.

For the local velocities, the translation velocities $_C \mathbf{v}_{C,i}$ as well as the angular velocity vector $_C \boldsymbol{\omega}_{C,i}$ of the center point of shaft C_1 and bearing C_2, respectively, are needed. With them, the following local velocities can be stated:

$$_C \begin{pmatrix} u \\ v \\ w \end{pmatrix}_i = {_C}\mathbf{v}_{C,i} + {_C}\boldsymbol{\omega}_{C,i} \times {_C}\mathbf{r}_{CP,i} + {_C}\dot{\boldsymbol{\delta}}_{CP,2}, \quad i \in \{1, 2\}, \tag{6}$$

with the local velocity $_C \dot{\boldsymbol{\delta}}_{CP,2}$ due to the vibration of the elastic bearing shell and with the distance vectors

$$_C \mathbf{r}_{CP,1} = \begin{pmatrix} \sqrt{R_1^2 - e_t^2(y, z)} \\ -e_t(y, z) \\ z \end{pmatrix}, \qquad _C \mathbf{r}_{CP,2} = \begin{pmatrix} h_2(y, z) \\ 0 \\ z \end{pmatrix}. \tag{7}$$

For the two-dimensional example in Fig. 2, the angular velocity vectors are $_C \boldsymbol{\omega}_{C,1} = (0,\ 0,\ \omega_1)^{\mathrm{T}}$ and $_C \boldsymbol{\omega}_{C,2} = (0,\ 0,\ \omega_2)^{\mathrm{T}}$.

Having the kinematic entities as a function of the descriptive coordinates (y, z), the derivatives of the local heights and velocities with respect to y can be derived for the REYNOLDS equation.

2.1.3 Cavitation condition

For the further calculation of the pressure, a cavitation condition is imposed on the REYNOLDS equation (1) in order to avoid unphysical negative pressures in the fluid film. Here, a stationary cavitation condition, also known as REYNOLDS condition, is applied. It states that in the pressurized zone ($p > 0$) the non-stationary density flux $q_{\text{exp.}} = h \frac{\partial \rho}{\partial t}$ is zero ($-q_{\text{exp.}} = 0$), whereas in the cavitation zone ($p = 0$) the density flux is positive ($-q_{\text{exp.}} > 0$), meaning the density starts to decrease. This cavitation condition can be formulated mathematically by a Linear Complementarity Problem (LCP) by finding the pressure p such that:

$$20 \leq -q_{\text{exp.}} = \left(-\nabla \left(\frac{h^3 \rho}{12\eta} \nabla p \right) + q_{\text{couette}} + q_{\text{squezze}} \right) \perp p \geq 0 \quad \text{on } \Omega_f, \tag{8}$$

$$p = \hat{p} \quad \text{on } \Gamma_p, \tag{9}$$

$$\frac{h^3 \rho}{12\eta} \nabla p \mathbf{n} = \hat{q} \quad \text{on } \Gamma_q, \tag{10}$$

where the symbol $\perp$ denotes orthogonality for each point (y, z) on Ω_f (i.e. $q_{\text{exp.}}(y, z) \cdot p(y, z) = 0$). Dirichlet and Neumann boundary conditions at the boundaries Γ_p and Γ_q, respectively, are considered additionally in the REYNOLDS equation by (9) and (10). In our case, the pressure is set to zero at the two bearing sides.

A numerical solution of equations (8) to (10) can be achieved by a finite element discretization. For the discretized pressure $\mathbf{P}$, the following discretized LCP is then obtained:

$$0 \leq \mathbf{P} \perp -\mathbf{Q}_{\text{exp.}} \geq 0 \quad \Leftrightarrow \quad 0 \leq \mathbf{P} \perp \mathbf{N}^{-1} \left[\mathbf{A(q)P} - \mathbf{b(q, \dot{q})} \right] \geq 0, \tag{11}$$

where the kinematics are described by the generalized coordinates $\mathbf{q}$ and velocities $\dot{\mathbf{q}}$ and the symbol $\perp$ stands now for component-wise orthogonality. The square matrix $\mathbf{A}$ results from the numerical discretization of the POISEUILLE term of Eq. (1), the vector $\mathbf{b}$ from the discretization of the terms $-q_{\text{couette}}$ and $-q_{\text{squeeze}}$ and square matrix $\mathbf{N}$ is the finite element mass matrix.

This resulting LCP for the pressure $\mathbf{P}$ can be solved by different methods, e.g. a block pivot-based Murty algorithm of Goenka [8] or a projection formulation as proposed in [17].

2.2 Force calculation

Having calculated the pressure $\mathbf{P}$ on the fluid mesh by Eq. (11), the forces on the two bodies can be computed. In this contribution, we want to describe only pressure forces in normal direction, but the methods can easily be extended to shear forces in tangential direction.

For the calculation, the pressure $\mathbf{P}_f$ is integrated on the fluid mesh, yielding the vector of discrete forces $\mathbf{F}_f$:

$$\mathbf{F}_f = \mathbf{M}_{ff} \mathbf{P}_f, \qquad M_{ff}^{jk} = \int_{\Omega_f} N_f^j(y, z) N_f^k(y, z) \mathbf{n}_f(y, z) \, d\Omega_f, \quad j, k = 1, \dots, m_f, \tag{12}$$

where $N_f(y, z)$ are the ansatz functions for both the pressure and the displacement field on the fluid mesh, $\mathbf{n}_f(y, z)$ is the local normal vector on the fluid mesh and m_f the number of nodes on the fluid mesh.

For a rigid body, the resulting force $\mathbf{F}_{res}$ is needed, which is obtained by the sum of the discrete forces:

$$\mathbf{F}_{res} = \sum_{m=1}^{m_f} \mathbf{F}_{f,m}. \tag{13}$$

For a flexible body with a structure mesh on its interface, which does not necessarily coincide with the fluid mesh, methods of fluid structure interaction have to be applied to transfer the pressure from one mesh to another. Here, the Mortar method [2] is chosen as a weighted residual approach, which gives a consistent transfer matrix $\mathbf{H}_{sf}$ between the pressure $\mathbf{P}_f$ of the fluid mesh and the pressure $\mathbf{P}_s$ of the structure mesh:

$$\mathbf{P}_s = \mathbf{H}_{sf} \, \mathbf{P}_f. \tag{14}$$

For the determination of $\mathbf{H}_{sf}$, it is referred to [6, 16]. Note that beside the Mortar method other methods for the construction of $\mathbf{H}_{sf}$ are applicable; see [6]. With the pressure $\mathbf{P}_s$ on the structure mesh, it is possible next to calculate the force vector $\mathbf{F}_s$ containing all forces at the single nodes of the interface mesh of the structure:

$$\mathbf{F}_s = \mathbf{M}_{ss}\mathbf{P}_s, \qquad M_{ss}^{li} = \int_{\Gamma_S} N_s^i(\mathbf{x}) N_s^l(\mathbf{x}) \mathbf{n}_s(\mathbf{x}) \, d\mathbf{x}, \quad l, i = 1, \ldots, m_s, \tag{15}$$

where $N_s(\mathbf{x})$ are the shape functions for both the pressure and the displacement field on the structure mesh, $\mathbf{n}_s(\mathbf{x})$ is the local normal vector on the structure mesh and m_s the number of nodes on the structure mesh. The interface Γ_S of the structure is described by coordinates $\mathbf{x}$.

3 Reduction methods

In this section, three different reduction methods for flexible structures with a lubricated interface are presented. The reduced structures are later used in a floating frame of reference formulation. It means that the shaft and the housing are considered as separate substructures that will be reduced.

All methods are described for a linear finite element model (N degrees of freedom) governed by the equation

$$\mathbf{M}_{FE}\ddot{\mathbf{x}} + \mathbf{K}_{FE}\mathbf{x} = \mathbf{f}(t) \tag{16}$$

with mass matrix $\mathbf{M}_{FE}$, stiffness matrix $\mathbf{K}_{FE}$ and a vector $\mathbf{f}(t)$ of external forces. For further considerations, the displacement vector $\mathbf{x}$ of the finite element model (16) is partitioned into n_i degrees of freedom of inner nodes, n_p degrees of freedom of the nodes of the lubricated interface and n_b degrees of freedom of boundary nodes, yielding:

$$\mathbf{x} = \begin{pmatrix} \mathbf{x}_i^T & \mathbf{x}_p^T & \mathbf{x}_b^T \end{pmatrix}^T. \tag{17}$$

In the first method, a CRAIG–BAMPTON procedure is applied, which does not particularly take care of the lubricated interface. The second method uses the CRAIG–BAMPTON method twice in sequence, in order to cover the deformation of the lubricated interface in a

better way. In contrast to the first two methods, which are based on fixed-interface modes, the third method describes a dual reduction scheme using vibration modes of the free floating structure, attachment modes and additionally load dependent static modes for the lubricated interface.

3.1 CRAIG–BAMPTON reduction (M1)

The first method is a classical CRAIG–BAMPTON reduction [1] without considering the lubricated interface in particular. Hence, the nodes $\mathbf{x}_p$ of the lubricated interface are treated like inner nodes, which leads to the following partitioned finite element system:

$$\begin{bmatrix} \mathbf{M}_{\bar{p}\bar{p}} & \mathbf{M}_{\bar{p}b} \\ \mathbf{M}_{b\bar{p}} & \mathbf{M}_{bb} \end{bmatrix} \begin{pmatrix} \ddot{\mathbf{x}}_{\bar{p}} \\ \ddot{\mathbf{x}}_b \end{pmatrix} + \begin{bmatrix} \mathbf{K}_{\bar{p}\bar{p}} & \mathbf{K}_{\bar{p}b} \\ \mathbf{K}_{b\bar{p}} & \mathbf{K}_{bb} \end{bmatrix} \begin{pmatrix} \mathbf{x}_{\bar{p}} \\ \mathbf{x}_b \end{pmatrix} = \begin{pmatrix} \mathbf{f}_{\bar{p}} \\ \mathbf{f}_b \end{pmatrix}, \tag{18}$$

with the partitioned displacement vector $\mathbf{x}_{\bar{p}} = (\mathbf{x}_i^{\mathrm{T}}\ \mathbf{x}_p^{\mathrm{T}})^{\mathrm{T}}$. The CRAIG–BAMPTON procedure gives the following reduction of the displacement vector:

$$\mathbf{x} = \begin{bmatrix} \boldsymbol{\Phi}_{\bar{p}\bar{v}} & -\mathbf{K}_{\bar{p}\bar{p}}^{-1}\mathbf{K}_{\bar{p}b} \\ \mathbf{0}_{b\bar{v}} & \mathbf{I}_{bb} \end{bmatrix} \begin{pmatrix} \mathbf{q}_{\bar{p}} \\ \mathbf{x}_b \end{pmatrix} = \mathbf{T} \begin{pmatrix} \mathbf{q}_{\bar{p}} \\ \mathbf{x}_b \end{pmatrix}, \tag{19}$$

where $\mathbf{q}_{\bar{p}}$ is the vector of the reduced modal coordinates, $\mathbf{I}_{bb}$ is the identity matrix and the matrix $\boldsymbol{\Phi}_{\bar{p}\bar{v}}$ contains a subset of the first $\bar{n}_v < n_i + n_p$ fixed-boundary vibration modes corresponding to the eigenvalue problem for the nodes $\mathbf{x}_{\bar{p}}$:

$$\left(-\omega_i^2 \mathbf{M}_{\bar{p}\bar{p}} + \mathbf{K}_{\bar{p}\bar{p}}\right)\boldsymbol{\phi}_i = \mathbf{0}, \quad i = 1, \ldots, (n_i + n_p) \tag{20}$$

with eigenvalues ω_i^2 and eigenvectors $\boldsymbol{\phi}_i$.

3.2 Two-step CRAIG–BAMPTON reduction (M2)

The second method, which is already used for mechanical systems with lubricated contacts [19], is decomposed into two steps.

In the first step, the nodes of the lubricated interface of system (16) are treated like boundary nodes and the CRAIG–BAMPTON procedure is applied, leading to the following transformation:

$$\mathbf{x} = \begin{bmatrix} \hat{\boldsymbol{\Phi}}_{i\hat{v}} & -\mathbf{K}_{ii}^{-1}\mathbf{K}_{ip} & -\mathbf{K}_{ii}^{-1}\mathbf{K}_{ib} \\ \mathbf{0}_{p\hat{v}} & \mathbf{I}_{pp} & \mathbf{0}_{pb} \\ \mathbf{0}_{b\hat{v}} & \mathbf{0}_{bp} & \mathbf{I}_{bb} \end{bmatrix} \begin{pmatrix} \mathbf{q}_i \\ \mathbf{x}_p \\ \mathbf{x}_b \end{pmatrix} = \mathbf{T}_1 \hat{\mathbf{x}}, \tag{21}$$

where the matrix $\hat{\boldsymbol{\Phi}}_{i\hat{v}}$ contains a subset of the first $\hat{n}_v < n_i$ fixed-interface vibration modes corresponding to the eigenvalue problem for the inner nodes $\mathbf{x}_i$. This first reduction step gives the reduced system matrices:

$$\mathbf{T}_1^{\mathrm{T}}\mathbf{M}_{\mathrm{FE}}\mathbf{T}_1 = \begin{bmatrix} \mathbf{I}_{\hat{v}\hat{v}} & \hat{\mathbf{M}}_{\hat{v}p} & \hat{\mathbf{M}}_{\hat{v}b} \\ \hat{\mathbf{M}}_{p\hat{v}} & \hat{\mathbf{M}}_{pp} & \hat{\mathbf{M}}_{pb} \\ \hat{\mathbf{M}}_{b\hat{v}} & \hat{\mathbf{M}}_{bp} & \hat{\mathbf{M}}_{bb} \end{bmatrix}, \qquad \mathbf{T}_1^{\mathrm{T}}\mathbf{K}_{\mathrm{FE}}\mathbf{T}_1 = \begin{bmatrix} \boldsymbol{\Omega}_{\hat{v}}^2 & \mathbf{0}_{\hat{v}p} & \mathbf{0}_{\hat{v}b} \\ \mathbf{0}_{p\hat{v}} & \hat{\mathbf{K}}_{pp} & \mathbf{0}_{pb} \\ \hat{\mathbf{K}}_{b\hat{v}} & \hat{\mathbf{K}}_{bp} & \hat{\mathbf{K}}_{bb} \end{bmatrix}. \tag{22}$$

In a second step, the already reduced system is further reduced by a second CRAIG–BAMPTON reduction step for the new coordinate vector $\hat{\mathbf{x}} = (\mathbf{q}_i^{\mathrm{T}}\ \mathbf{x}_p^{\mathrm{T}}\ \mathbf{x}_b^{\mathrm{T}})^{\mathrm{T}}$. Maintaining the

boundary nodes $\mathbf{x}_b$, the second transformation is given by

$$
\hat{\mathbf{x}} = \begin{bmatrix} \boldsymbol{\Phi}_{\hat{v}\tilde{v}} & \mathbf{0}_{\hat{v}b} \\ \boldsymbol{\Phi}_{p\tilde{v}} & \mathbf{0}_{pb} \\ \mathbf{0}_{b\tilde{v}} & \mathbf{I}_{bb} \end{bmatrix} \begin{pmatrix} \mathbf{q}_{\bar{p}} \\ \mathbf{x}_b \end{pmatrix} = \mathbf{T}_2 \begin{pmatrix} \mathbf{q}_{\bar{p}} \\ \mathbf{x}_b \end{pmatrix}.
\tag{23}
$$

The matrix $\begin{bmatrix} \boldsymbol{\Phi}_{\hat{v}\tilde{v}}^{\mathrm{T}} & \boldsymbol{\Phi}_{p\tilde{v}}^{\mathrm{T}} \end{bmatrix}^{\mathrm{T}}$ contains a subset of the first $\tilde{n}_v < \hat{n}_v + n_p$ fixed-boundary vibration modes computed from the reduced system (22), where the boundary degrees of freedom are fixed, namely

$$
\left(-\omega_i^2 \begin{bmatrix} \mathbf{I}_{\hat{v}\hat{v}} & \hat{\mathbf{M}}_{\hat{v}p} \\ \hat{\mathbf{M}}_{p\hat{v}} & \hat{\mathbf{M}}_{pp} \end{bmatrix} + \begin{bmatrix} \boldsymbol{\Omega}_{\hat{v}\hat{v}}^2 & \mathbf{0}_{\hat{v}p} \\ \mathbf{0}_{p\hat{v}} & \hat{\mathbf{K}}_{pp} \end{bmatrix} \right) \boldsymbol{\phi}_i = \mathbf{0}, \quad i = 1, \ldots, (\hat{n}_v + n_p).
\tag{24}
$$

This second reduction step couples the static interface modes with the fixed-interface vibration modes of the first step. In conclusion, the complete procedure of the second method is expressed by the reduction basis $\mathbf{T}$, see (21) and (23):

$$
\mathbf{x} = \mathbf{T} \begin{pmatrix} \mathbf{q}_{\bar{p}} \\ \mathbf{x}_b \end{pmatrix}, \qquad \mathbf{T} = \mathbf{T}_1 \mathbf{T}_2.
\tag{25}
$$

After the complete reduction sequence, the reduced matrices at the end will be block-diagonal like in the classical CRAIG–BAMPTON case, since the second step is like applying CRAIG–BAMPTON on the reduced problem (22) of the first step.

3.3 Load dependent reduction strategy (M3)

In this section, a load dependent reduction strategy is proposed. The general framework of the procedure is based on a dual superelement formulation of [7]. Therefore, for a more detailed description of the surrounding framework, it is referred to [7] and here, only the main steps of the procedure and its specification for lubricated interfaces are given.

3.3.1 General framework

In [7], for the finite element system (16), a reduction basis

$$
\mathbf{V} = \begin{bmatrix} \mathbf{U} & \boldsymbol{\Phi}_v & \mathbf{G}_a & \mathbf{G}_r \end{bmatrix} = \begin{bmatrix} \mathbf{U} & \mathbf{T} \end{bmatrix}
\tag{26}
$$

is proposed. The matrix $\mathbf{U}$ collects the n_u rigid body modes of the floating structure, the matrix $\boldsymbol{\Phi}_v$ collects the n_v vibration modes of the free floating structure (usually $n_v \ll (N - n_u)$), the matrix $\mathbf{G}_a$ collects the n_a attachment modes obtained by the static responses of a unit loading at the attachment nodes and the matrix $\mathbf{G}_r$ collects n_r residual modes, which can be chosen in different ways in order to enrich the reduction basis, e.g. in the case of nonlinear external forces like contact forces. In this contribution, the set of residual modes will be created by static responses due to pressure forces (see below).

The eigenvalue problem of system (16),

$$
\begin{aligned}
\left(-\omega_i^2 \mathbf{M}_{\mathrm{FE}} + \mathbf{K}_{\mathrm{FE}} \right) \boldsymbol{\phi}_i &= \mathbf{0} \quad i = 1, \ldots, N, \\
\rightarrow \quad \text{rigid body modes:} \quad \mathbf{U} &= \begin{bmatrix} \boldsymbol{\phi}_1, \ldots, \boldsymbol{\phi}_{n_u} \end{bmatrix} \quad \text{for } \omega_i^2 = 0, \\
\rightarrow \quad \text{vibration modes:} \quad \boldsymbol{\Phi}_v &= \begin{bmatrix} \boldsymbol{\phi}_{n_u+1}, \ldots, \boldsymbol{\phi}_{n_u+n_v} \end{bmatrix} \quad \text{for } \omega_i^2 \neq 0,
\end{aligned}
\tag{27}
$$

gives the n_u rigid body modes belonging to the zero eigenvalues and the $(N - n_u)$ vibration modes belonging to the remaining eigenvalues. A modal reduction is obtained, when only a reduced set of $n_v < (N - n_u)$ vibration modes is used. The vibration modes can be mass normalized in such a way that

$$\boldsymbol{\Phi}_v^{\mathrm{T}} \mathbf{K}_{\mathrm{FE}} \boldsymbol{\Phi}_v = \boldsymbol{\Omega}_v^2, \qquad \boldsymbol{\Phi}_v^{\mathrm{T}} \mathbf{M}_{\mathrm{FE}} \boldsymbol{\Phi}_v = \mathbf{I}_{vv}. \tag{28}$$

For the n_a attachment modes, a loading matrix $\mathbf{J}_a$ is constructed, in which each column belongs to a unit force vector at a single attachment node. In a similar way, for the residual modes, a loading set $\mathbf{J}_c$ is constructed, which contains n_c arbitrary load cases not necessarily being unit force vectors or belonging to an attachment node. The static responses $\mathbf{G}_a$ and $\mathbf{G}_c$ are calculated by solving

$$\begin{bmatrix} \mathbf{K}_{\mathrm{FE}} & \mathbf{M}_{\mathrm{FE}}\mathbf{U} \\ \mathbf{U}^{\mathrm{T}}\mathbf{M}_{\mathrm{FE}} & \mathbf{0} \end{bmatrix} \begin{bmatrix} \mathbf{G}_a & \mathbf{G}_c \\ \lambda_a & \lambda_c \end{bmatrix} = \begin{bmatrix} \mathbf{J}_a & \mathbf{J}_c \\ \mathbf{0} & \mathbf{0} \end{bmatrix}, \tag{29}$$

where the LAGRANGE multiplier λ_a and λ_c ensure mass orthogonality of the static mode sets with respect to the rigid body modes.

The directions of the static mode set $[\mathbf{G}_a \ \mathbf{G}_c]$, which are already covered by the vibration modes $\boldsymbol{\Phi}_v$, are filtered out by the following transformation:

$$\begin{bmatrix} \mathbf{G}_a & \mathbf{G}_c \end{bmatrix} \leftarrow \begin{bmatrix} \mathbf{G}_a & \mathbf{G}_c \end{bmatrix} - \boldsymbol{\Phi}_v \boldsymbol{\Omega}_v^{-2} \boldsymbol{\Phi}_v^{\mathrm{T}} \begin{bmatrix} \mathbf{J}_a & \mathbf{J}_c \end{bmatrix}. \tag{30}$$

A reduced set $\mathbf{G}_r$ of residual modes can be obtained from the static set $\mathbf{G}_c$ by different approaches, e.g. by selecting these modes, which contribute the most to the strain energy. In this contribution, they are computed by an eigenvalue problem for the reduced stiffness matrix $\mathbf{K}_{cc} = \mathbf{G}_c^{\mathrm{T}} \mathbf{K}_{\mathrm{FE}} \mathbf{G}_c$:

$$\left(-\omega_i^2 \mathbf{I}_{cc} + \mathbf{K}_{cc} \right) \mathbf{Z}_i = \mathbf{0}, \quad i = 1, \ldots, n_c, \tag{31}$$

and choosing the set of eigenvectors $\mathbf{Z}_r$ belonging to the first n_r smallest eigenvalues ω_i^2. Then a reduction of the static modes $\mathbf{G}_c$ is achieved by the following transformation:

$$n_r \leftarrow n_c, \qquad \mathbf{G}_r \leftarrow \mathbf{G}_c \mathbf{Z}_r, \qquad \boldsymbol{\Omega}_r^2 \leftarrow \mathbf{K}_{cc}. \tag{32}$$

Thus far, a reduction by the transformation matrix $\mathbf{T}$ of (26) not yet gives a nicely block-diagonal form for the reduced matrices. However, such a form can be achieved by applying further diagonalization steps as described in [7].

3.3.2 Construction of interface modes

The set $\mathbf{G}_r$ of the static residual modes is a subset of the static set $\mathbf{G}_c$, which is defined by an arbitrary load set $\mathbf{J}_c$; see (29) and (32). In the following, the load set $\mathbf{J}_c$ is specified for pressure forces coming from the hydrodynamic equations of Sect. 2. With (15), it is generally defined by

$$\mathbf{J}_c = \mathbf{M}_{ss} \mathbf{P}_c, \tag{33}$$

where $\mathbf{P}_c$ is a set of discrete pressure values. Setting

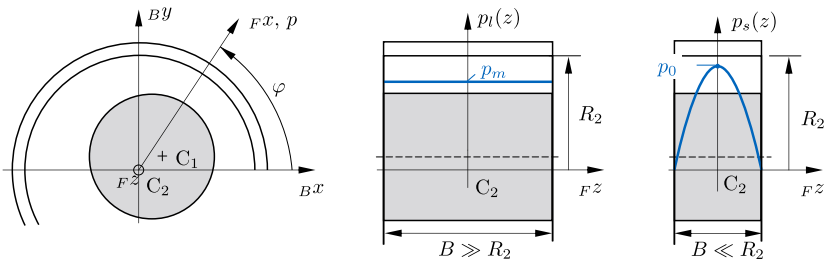$$\mathbf{P}_{c,1} = \mathbf{I}_{cc} \tag{34}$$

Fig. 3 Pressure distributions for infinitely long (*middle*) and infinitely short bearing (*right*), computed in a discrete ($_F x$, $_F z$)-plane (*left*)

to the identity matrix, gives an overall definition of the pressure set, as unit pressure values are applied at the interface nodes. This choice already reduces the $3m_s$ degrees of freedom of the interface to m_s degrees of freedom, since the pressure forces are acting in normal direction only.

As the number m_s still can be large, we propose to build a set of pressure distribution, which is applicable for lubricated revolute joints, where the relative rotation occurs around the $_F z$-direction only (no tilting), like in Fig. 2. In this case, analytical solutions for the pressure distribution in $_F z$-direction exist for an infinite long and an infinite short bearing; see Fig. 3. The solution $p_l(z)$ of an infinite long bearing gives a constant pressure distribution and the solution $p_s(z)$ of an infinite short bearing gives a quadratic distribution:

$$p_l(z) = p_m, \qquad p_s(z) = \frac{4p_0}{B^2}\left(\frac{B^2}{4} - z^2\right),$$

where B is the bearing width and the mean pressure p_m of the long and the maximal pressure p_0 of the short bearing solution, respectively, still have to be specified in the circumferential direction. We propose to build a set of pressure distribution by assuming the analytical axial distribution at several circumferential positions:

$$\mathbf{P}_{c,2} = \begin{bmatrix} \mathbf{P}_{l,1} & \dots & \mathbf{P}_{l,m_{sy}}, & \mathbf{P}_{s,1} & \dots & \mathbf{P}_{s,m_{sy}} \end{bmatrix}. \tag{35}$$

With this pressure set $\mathbf{P}_{c,2}$, the $3m_s$ interface degrees of freedom are reduced to $2m_{sy}$ from the beginning.

4 Simulation example 1: flexible slider–crank mechanism

In this section, the described reduction methods are compared for a simulation example of a slider–crank mechanism with an elastic connecting rod between a rigid crank shaft and a rigid piston. Hence, the connecting rod is the only body with flexible behavior. This simplification is made in order to better demonstrate and compare the different reduction methods. Further, when assuming the crank shaft to be rigid, there is no need for dealing with sliding meshes, which would be a topic beyond of this contribution.

4.1 Flexible slider–crank mechanism

The flexible slider–crank mechanism is shown in Fig. 4. A hydrodynamic revolute cylindrical joint links the rigid shaft with the flexible connecting rod. A constant rotation
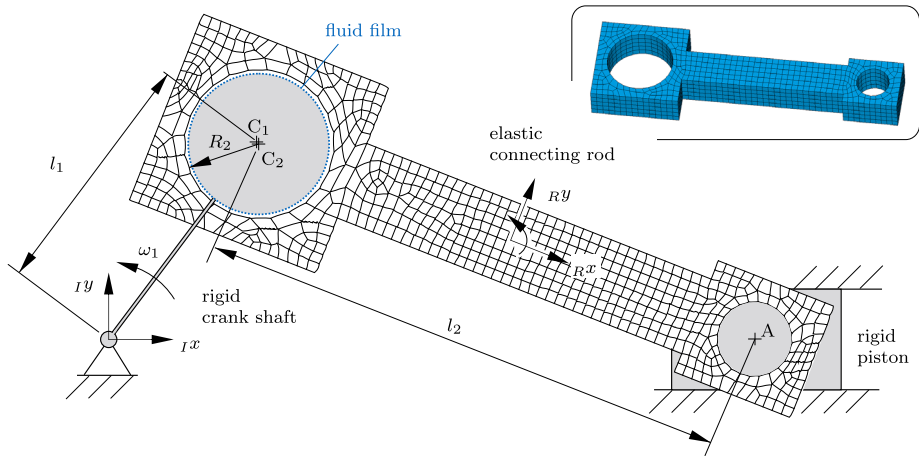
Fig. 4 Slider–crank mechanism with 3D flexible connecting rod and lubricated joint

speed $\omega_1 = 500$ rad/s around the initial $_Iz$-direction is enforced. At the beginning of the simulation, the slider is positioned at $_Ix = l_1 + l_2$, i.e. the relative eccentricity in the bearing is zero. Note that the elastic structure deforms three-dimensionally, while the main rigid body motion of the rod takes place in the $_Ix/_Iy$-plane. Due to the rotation around the $_Iz$-axis only, the concept of combining the short and long bearing solutions in the third reduction scheme is well applicable. The more general case will be considered in Sect. 5 model occurs in the two-dimensional $(_Ix, _Iy)$-plane

The mass and stiffness matrix of the 3D flexible rod come from a finite element software tool. They are embedded in the multi-body simulation by a floating frame of reference formulation as described in [4, 15, 21]. For the first two CMS-based reduction methods, the floating frame is automatically attached to the center C_2 of the hydrodynamic bearing by constraining the rigid body translation and rotation of point C_2. For the third reduction method, where a dual approach is followed and free-interface normal modes are used, the floating frame is automatically located in the deformed configuration of the center of mass, also known as mean axis or Tisserant frame [21].

The cylindrical interface for the bearing is meshed with 20×5 bi-quadratic elements in circumferential and z-direction, respectively, which results in $m_s = 340$ interface nodes on the structure with $m_{sy} = 40$ equally distributed circumferential positions. Structural damping is applied by choosing the reduced damping matrix $\mathbf{D}_e = \zeta(\mathbf{T}^T\mathbf{K}_{FE}\mathbf{T})$ proportional to the reduced stiffness matrix with damping factor ζ. For the fluid mesh, a structured mesh with 20×5 bi-quadratic elements in circumferential and z-direction, respectively, is used, leading to $m_f = 340$ fluid nodes. The fluid mesh is assumed to be attached to the housing, meaning it is always conforming with the structural mesh. Further simulation parameters and fluid properties are listed in Table 1.

4.2 Comparison of the three reduction methods

Global simulation outputs of the flexible slider–crank mechanism are compared for the three reduction methods of Sect. 3. In detail, the maximal pressure and the minimal height during one rotation, i.e. $T = 2\pi/\omega_1$, are analyzed.

Table 1 Simulation parameters for the slider crank mechanism

Parameter	Value	Parameter	Value
Angular velocity ω_1	500 rad/s	dyn. viscosity η	0.01 kg/m s
Radius bearing R_2	2.25 cm	fluid density ρ_0	800 kg m^3
Clearance $h_0 = R_2 - R_1$	17.0 μm	nb. fluid nodes m_f	340
Bearing width B	2.20 cm	nb. interface nodes m_s	340
Crank length l_1	0.048 m	damping factor ζ	0.001
Rod length l_2	0.160 m	E-module E	210×10^9 N m^2
Rod center of mass $c_{2,x}$	0.0677 m	tolerances tol_{Abs}, tol_{Rel}	1×10^{-7}
Crank mass m_1	1.00 kg	crank inertia $J_{1,zz}$	1×10^{-3} kg m^2
Rod mass m_2	0.973 kg	rod inertia $J_{2,zz}$	4×10^{-3} kg m^2
Piston mass m_3	0.500 kg		

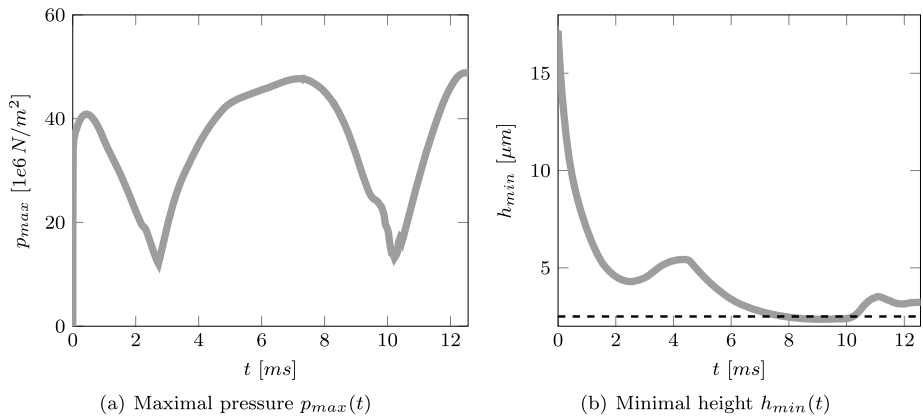(a) Maximal pressure $p_{max}(t)$ (b) Minimal height $h_{min}(t)$

Fig. 5 Reference solution with (M3) by using $\mathbf{P}_{c,1} = \mathbf{I}_{cc}$, $n_r = 60$ residual modes and $n_v = 6$ vibration modes

A reference solution is created with the third reduction method (M3) by applying the general choice $\mathbf{P}_{c,1} = \mathbf{I}_{cc}$ for the pressure set. A large number of $n_r = 60$ residual modes is used ensuring a reduction basis, which is rich enough to cover the interface behavior. The maximal pressure and minimal height over time are shown in Figs. 5(a) and 5(b). The number of vibration modes is $n_v = 6$. In Fig. 5(b), a typical value $h_{safe} \approx 2.5$ μm for the safe height in engine bearings is depicted as well [18]. In the reference solution, an interesting effect due to the elasticity of the journal bearing can be observed: Between $t = 6$ to 8 ms, the maximal pressure is almost constant, while the minimum film thickness is decreasing. Note that the maximum pressure can be found at $\varphi \approx 0$ in the flexible bearing. In this zone, the pressure distribution changes from a sharp to a more smoother profile in the divergent fluid zone, since the flexibility of the bearing increases at $\varphi = 0$ in circumferential direction. This effect causes the maximal pressure to remain constant, while the minimum film thickness is decreasing.

In order to compare the three methods, the results of the maximal pressure and the minimal height are analyzed for a comparable number of modes. Point A of the flexible rod is considered as a boundary node in the reduction methods M1 and M2 and as a attachment
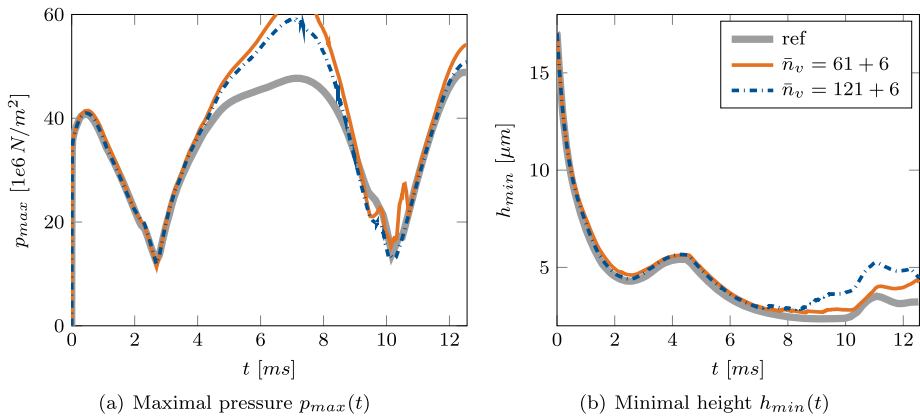
(a) Maximal pressure $p_{max}(t)$

(b) Minimal height $h_{min}(t)$

Fig. 6 CRAIG–BAMPTON scheme (M1)

(a) Maximal pressure $p_{max}(t)$
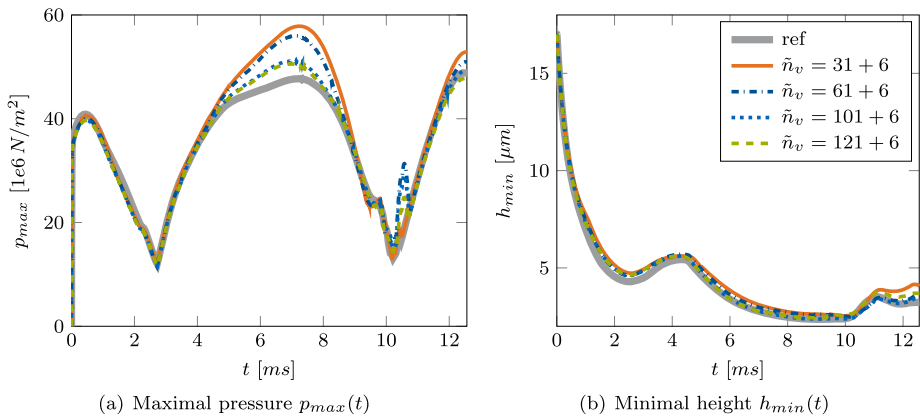
(b) Minimal height $h_{min}(t)$

Fig. 7 Two-step CRAIG–BAMPTON scheme (M2)

mode in method M3, respectively. In the first two methods, $n_b = 2$ static deformation modes and in the third method, $n_a = 2$ attachment modes, respectively are used by applying unit displacements and unit forces in $_R x / _R y$-direction, respectively. For the load dependent reduction method (M3), it can be well distinguished between vibration modes and residual modes, which allows us to use a fixed number of 6 vibration modes ($n_v = 6$) and vary the number n_r of residual modes. For the two-step CRAIG–BAMPTON method (M2), the number of overall vibration modes is varied in dependence of n_r by $\tilde{n}_v = n_r + 6$. Making the CRAIG–BAMPTON method (M1) comparable as well, the number $\bar{n}_v$ of vibration modes is varied in the same way, yielding $\bar{n}_v = n_r + 6$.

In Fig. 6, the results for the first reduction method (M1) are shown. Compared to the reference solution, its obvious that a large number of modes is required to cover the interface deformation. In particular, in the segments of high loads of Fig. 6(a), the pressure is overestimated, as the reduction basis is too poor.

Figure 7 shows the maximal pressure and minimal height obtained by the second reduction method (M2). Compared to M1, for similar results, less modes are required. However, the number $\tilde{n}_v$ of modes has still to be large, when the reference solution should be well ap-

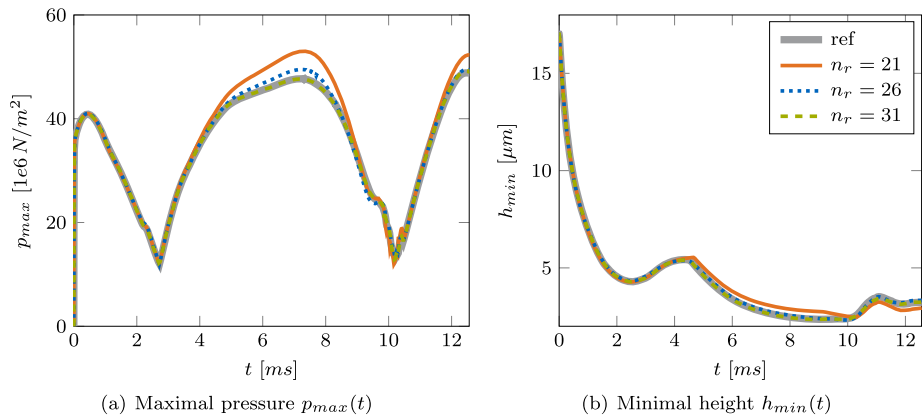(a) Maximal pressure $p_{max}(t)$ (b) Minimal height $h_{min}(t)$

Fig. 8 Load dependent reduction scheme (M3) with $\mathbf{P}_{c,2}$ ($p_m = 1$ and $p_0 = 1.5$)

proximated. As can be seen in Fig. 7(a), the elastic structure with $\tilde{n}_v = 127$ modes behaves still too stiff in the high pressure segments.

The maximal pressure and minimal height for the load dependent reduction scheme (M3) with $\mathbf{P}_{c,2}$ are depicted in Fig. 8. The analytical pressure distributions in $_F z$-direction of the bearing width are normalized by setting $p_m = 1$ and $p_0 = 1.5$. It becomes clear that the reference solution is well approximated when using $n_r = 31$ residual modes only. Compared to M2, for similar results, less than a quarter of the number of modes are required. It is noteworthy that the combination of short and long bearing solution like in Eq. (35) is mainly necessary in order to account properly for the bending deformation of the bearing in $_F z$-direction. The application of only one of the two analytical solutions would not converge to the reference solution.

All the simulations are performed with Matlab on a i3-3220 CPU (3.3 GHz, 8 GB RAM). Concerning computational efficiency, it is noted that the computational time of the dynamic simulation strongly depends on the number of modes used for the description of the elastic body. Since the third reduction method needs at the same accuracy much less static modes than the first two reduction schemes do, the simulation time is relatively low when using the third reduction approach.

5 Simulation example 2: elastic rotor in flexible journal bearing

In this section, the second simulation example of an elastic rotor in a flexible journal bearing is analyzed. In contrast to the simulation example of the previous section, unsymmetrical pressure distributions along the axial direction now occur in the journal bearing. Again, the three reduction methods are compared with each other.

5.1 Elastic rotor in flexible journal bearing

The simulation model of the elastic rotor in the flexible journal bearing is depicted in Fig. 9.

The elastic rotor consist of an elastic shaft with a rigidly attached disk in the middle. The shaft is modeled by 20 BERNOULLI beam elements, each with two nodes and 4 degrees of freedom per node for the bending deformation in x- and y-direction, respectively. A modal
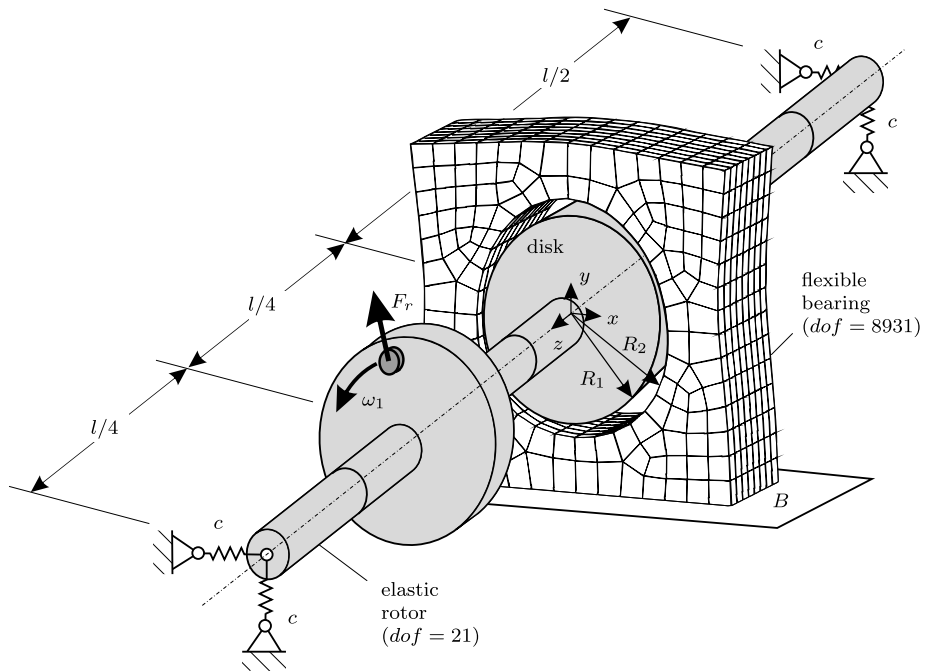
Fig. 9 Elastic rotor with unbalance in flexible journal bearing

reduction gives 20 modes for the elastic deformation of the rotor, leading together with the shaft rotation to 21 overall degrees of freedom. Gyroscopic effects are considered; see for instance [4]. The rotor with the length l is supported at both ends elastically by a stiffness c and at half length by a flexible journal bearing. Modal damping with the damping ratio ζ for each mode is considered. The rotor rotates with a constant rotation speed $\omega_1 = 600$ rad/s and at three quarter length of the rotor an unbalance force F_r acts in radial direction.

The flexible bearing housing is modeled as a 3D linear finite element system ($N = 8931$) with mass and stiffness matrix coming from a finite element software tool. Damping in the bearing housing is not considered. The cylindrical interface of the bearing consists of 20×5 bi-quadratic elements in circumferential and z-direction, respectively, leading to $m_s = 340$ interface nodes on the structure with $m_{sy} = 40$ circumferential positions. A conformal mesh is applied to the fluid zone, resulting in $m_f = 340$ fluid nodes.

In summary, the elastic structure deforms three-dimensionally and the rotor performs a bending motion in the x/y-plane while rotating around the initial z-axis. This motion results in unsymmetrical 3D pressure distributions in the journal bearing.

Further simulation parameters of the rotor model and the fluid properties are listed in Table 2.

5.2 Comparison of the three reduction methods

For the simulation example, the maximal pressure and minimal height are compared for the three reduction methods. The simulation time is $T = 2\pi/\omega$, meaning that one rotation is analyzed. In contrast to the simulation example of the slider–crank mechanism, unsymmetrical pressure distributions in axial direction now occur due to small tilting of the rotor shaft

Table 2 Simulation parameters for the elastic rotor in flexible journal bearing

Parameter	Value	Parameter	Value
Angular velocity ω_1	600 rad/s	dyn. viscosity η	0.01 kg/m s
Radius bearing R_2	2.25 cm	fluid density ρ_0	800 kg/m^3
Clearance $h_0 = R_2 - R_1$	17.0 μm	nb. fluid nodes m_f	340
Bearing width B	2.20 cm	nb. interface nodes m_s	340
Rotor length l	1.00 m	damping factor ζ	0.001
Rotor diameter d_r	2.25 cm	E-module E	210×10^9 N/m^2
Steel density ρ_r	7446 kg/m^3	simulation time T	$2\pi/\omega_1$
Rotor inertia $J_{r,zz}$	1×10^{-3} kg m^2	tolerances tol_{Abs}, tol_{Rel}	1×10^{-8}
Stiffness c	1.58×10^8 N m	radial force F_r	3.60 kN

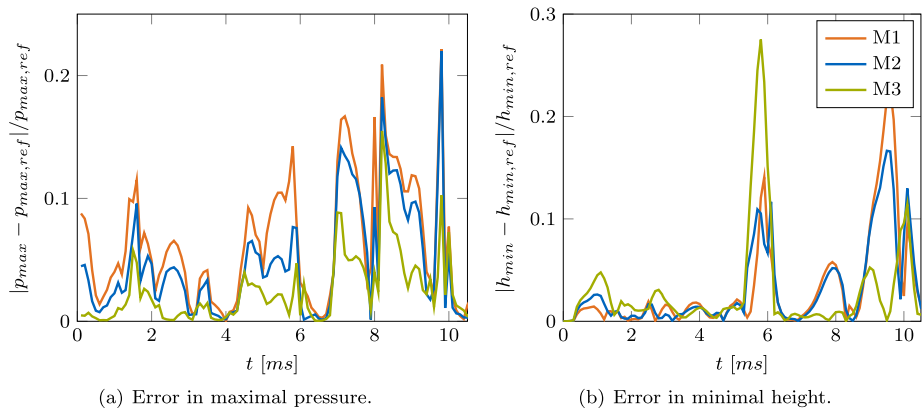(a) Error in maximal pressure.

(b) Error in minimal height.

Fig. 10 Comparison of the three reduction methods, each with 30 overall modes (Color figure online)

around the x- and y-directions, respectively. Therefore, the load dependent method (M3) is applied with the more general choice $\mathbf{P}_{c,1}$; see Eq. (34).

Similar to Sect. 4.2, the three reduction methods are compared for a comparable number of modes. For the load dependent method (M3), $n_v = 10$ vibration modes are used and the number n_r of residual modes is varied. For the two-step CRAIG–BAMPTON method (M2), the number $\tilde{n}_v$ of overall modes is chosen in dependence of n_r by $\tilde{n}_v = n_r + 10$. In a similar way, the number $\bar{n}_v$ of overall modes of the CRAIG–BAMPTON method (M1) is chosen by $\bar{n}_v = n_r + 10$.

A reference solution is created by considering the full interface. In Fig. 10, the error in the maximal pressure and minimal height are shown for all the three methods by using for each method 30 modes, which for the third method are decomposed into $n_r = 20$ residual and $n_v = 10$ vibration modes. It can be seen that the error in the maximal pressure is large, especially in time intervals which belong to high pressure situations. However, it becomes clear that the load dependent method M3 comes closer to the reference solution than the two CMS-based methods. The classical CRAIG–BAMPTON method (M1) shows the largest deviations. In Fig. 11, the number of residual modes n_r in method M3 is increased to 40, leading to 50 overall modes. While the first two methods still behave too stiff, the error by the third method is relatively small.
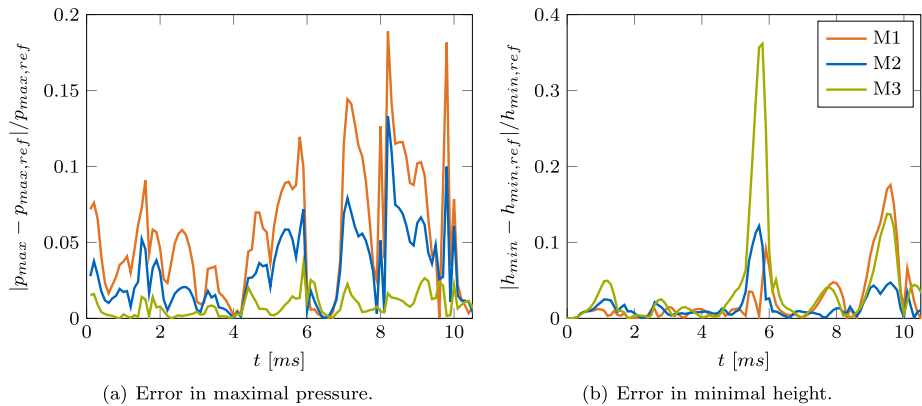
(a) Error in maximal pressure.

(b) Error in minimal height.

Fig. 11 Comparison of the three reduction methods, each with 50 overall modes (Color figure online)

6 Conclusion

Different reduction schemes for structures with lubricated interfaces are presented and compared for classical simulation examples.

The first two reduction methods are based on classical component mode synthesis. The first method does not take into account the lubricated interface in particular. The second method—a two-step CRAIG–BAMPTON scheme—gives a reduced set of modes by combining static interface deformation and the vibration modes of a interface-fixed structure. By this, the interface deformation is covered in a better way, but still a large number of modes is required.

The best results are obtained by a load dependent reduction strategy, where the interface modes are computed as static responses due to pressure forces. Within this dual approach, it is possible to use analytical pressure distributions like the infinitely short and long bearing solution. These analytical solutions are well applicable during the reduction process for 3D elastic revolute joints with a shaft rotating around one axis only, as the example of the slider crank mechanism demonstrates. A more general choice is required when unsymmetrical pressure distributions occur, like in the example of a flexible rotor in a flexible bearing housing.

As a further advantage, this load dependent reduction strategy allows a clear decomposition of vibration modes of the free floating structure and static modes belonging to attachment points and interface nodes. As a consequence, the number of modes for the lubricated interface can be adjusted independently of the vibration modes.

References

1. Bampton, M.C., Craig, R.R.: Coupling of substructures for dynamic analyses. AIAA J. **6**(7), 1313–1319 (1968)
2. Bernardi, C.: A new nonconforming approach to domain decomposition: the mortar element method. In: Nonlinear Partial Differential Equations and Their Applications. Wiley, New York (1994)
3. Booker, J., Boedo, S., Bonneau, D.: Conformal elastohydrodynamic lubrication analysis for engine bearing design: a brief review. Proc. Inst. Mech. Eng., Part C, J. Mech. Eng. Sci. **224**(12), 2648–2653 (2010)
4. Bremer, H.: Elastic Multibody Dynamics. Springer, Berlin (2008)
5. Craig, R.R., Chang, C.J.: Substructure coupling for dynamic analysis and testing. Tech. rep., University of Texas, Austin (1977)

6. De Boer, A.: Computational fluid–structure interaction: spatial coupling, coupling shell and mesh deformation. Ph.D. thesis, TU Delft, Delft University of Technology (2008)
7. Géradin, M., Rixen, D.J.: A 'nodeless' dual superelement formulation for structural and multibody dynamics application to reduction of contact problems. Int. J. Numer. Methods Eng. **106**(10), 773–798 (2015)
8. Goenka, P.K.: Dynamically loaded journal bearings: finite element method analysis. J. Tribol. **106**(4), 429–437 (1984)
9. Habchi, W.: Reduced order finite element model for elastohydrodynamic lubrication: circular contacts. Tribol. Int. **71**, 98–108 (2014)
10. Habchi, W., Issa, J.: Fast and reduced full-system finite element solution of elastohydrodynamic lubrication problems: Line contacts. Adv. Eng. Softw. **56**, 51–62 (2013)
11. Hamrock, B.J., Schmid, S.R., Jacobson, B.O.: Fundamentals of Fluid Film Lubrication. CRC press, New York (2004)
12. Herrmann, J., Maess, M., Gaul, L.: Substructuring including interface reduction for the efficient vibro-acoustic simulation of fluid-filled piping systems. Mech. Syst. Signal Process. **24**(1), 153–163 (2010)
13. Junge, M., Brunner, D., Becker, J., Gaul, L.: Interface-reduction for the Craig–Bampton and rubin method applied to Fe–Be coupling with a large fluid–structure interface. Int. J. Numer. Methods Eng. **77**(12), 1731–1752 (2009)
14. Knoll, G., Schönen, R., Wilhelm, K.: Full dynamic analysis of crankshaft and engine block with special respect to elastohydrodynamic bearing coupling. ASME ICE **28**(3), 1–8 (1997)
15. Krinner, A., Rixen, D.J.: Load dependent interface reduction method for flexible multibody systems with elastohydrodynamic lubricated joints. In: The 4th Joint International Conference on Multibody Dynamics May 29–June 2, Montreal, Canada (2016)
16. Krinner, A., Schindler, T., Rixen, D.J.: Fluid–struktur-kopplung in elastohydrodynamischen gleitlagern. In: 11. Internationale Tagung Schwingungen in Rotierenden Maschinen (SIRM), Magdeburg, Germany (2015), in German
17. Krinner, A., Schindler, T., Rixen, D.: Time integration of mechanical systems using quasi-newton method and projection formulations. Int. J. Numer. Methods Eng. **110**(6), 523–548 (2017). doi:10.1002/nme.5365
18. Lang, O.R., Steinhilper, W.: Gleitlager: Berechnung und Konstruktion von Gleitlagern mit konstanter und zeitlich veränderlicher Belastung, vol. 31. Springer, Berlin (1978)
19. Novotny, P., Pistek, V.: New efficient methods for powertrain vibration analysis. Proc. Inst. Mech. Eng., Part D, J. Automob. Eng. **224**(5), 611–629 (2010)
20. Oh, K., Goenka, P.: The elastohydrodynamic solution of journal bearings under dynamic loading. J. Tribol. **107**(3), 389–394 (1985)
21. Schwertassek, R., Wallrapp, O.: Dynamik flexibler Mehrkörpersysteme. Vieweg, Braunschweig (1999), in German
22. Tamarozzi, T., Heirman, G.H., Desmet, W.: An on-line time dependent parametric model order reduction scheme with focus on dynamic stress recovery. Comput. Methods Appl. Mech. Eng. **268**, 336–358 (2014)
23. Tian, Q., Sun, Y., Liu, C., Hu, H., Flores, P.: Elastohydrodynamic lubricated cylindrical joints for rigid-flexible multibody dynamics. Comput. Struct. **114**, 106–120 (2013)
24. Tian, Q., Lou, J., Mikkola, A.: A new elastohydrodynamic lubricated spherical joint model for rigid-flexible multibody dynamics. Mech. Mach. Theory **107**, 210–228 (2017)